
Article:
Yokoyama, T., Taguchi, A., Kubota, H. et al. (2019) Simultaneous T2* mapping of 14N- and 15N-labeled dicarboxy-PROXYLs using CW-EPR-based single-point imaging. Journal of Magnetic Resonance, 305. pp. 122-130. ISSN: 1090-7807

https://doi.org/10.1016/j.jmr.2019.06.012

Manuscript No. JMR-19-77R1

Simultaneous T_2^* mapping of ^{14}N- and ^{15}N-labeled dicarboxy-PROXYLs using CW-EPR-based single-point imaging

Takahito Yokoyama[a], Akihiro Taguchi[a], Harue Kubota[a], Neil J. Stewart[a], Shingo Matsumoto[a], Igor A. Kirilyuk[b], Hiroshi Hirata[a,*]

[a] Division of Bioengineering and Bioinformatics, Graduate School of Information Science and Technology, Hokkaido University, North 14, West 9, Kita-ku, Sapporo, 060-0814, Japan

[b] N. N. Vorozhtsov Novosibirsk Institute of Organic Chemistry, 9, Ac. Lavrentieva Ave., Novosibirsk, 630090, Russia

* Corresponding author:

Hiroshi Hirata, Ph.D.
Division of Bioengineering and Bioinformatics
Graduate School of Information Science and Technology
Hokkaido University
North 14, West 9, Kita-ku, Sapporo, 060-0814, Japan
Phone +81-11-706-6762
E-mail hhirata@ist.hokudai.ac.jp

Abstract

This article reports a method of simultaneous T_2^* mapping of ^{14}N- and ^{15}N-labeled dicarboxy-PROXYLs using 750-MHz continuous-wave electron paramagnetic resonance (CW-EPR) imaging. To separate the spectra of ^{14}N- and ^{15}N-labeled dicarboxy-PROXYLs under magnetic field gradients, an optimization problem for spectral projections was formulated with the spatial total variation as a regularization term and solved using a local search based on the gradient descent algorithm. Using the single-point imaging (SPI) method with spectral projections of each radical, simultaneous T_2^* mapping was performed for solution samples. Simultaneous T_2^* mapping enabled visualization of the response of T_2^* values to the level of dissolved oxygen in the solution. Simultaneous T_2^* mapping applied to a mouse tumor model demonstrated the feasibility of the reported method for potential application to *in vivo* oxygenation imaging.

(128 words)

Keywords: EPR, T_2^* mapping, nitroxyl radical, single-point imaging, gradient-descent optimization, oxygenation

Declaration of interest: none.

Funding: This work was supported by JSPS KAKENHI Grant Number JP26249057 and Ministry of Education and Science of the Russian Federation, grant 14.W03.31.0034.

1. Introduction

The partial pressure of oxygen (pO_2) in tumor tissues is a critical parameter of the tumor microenvironment and has significant impact on the outcomes of radiotherapy and anti-cancer drugs [1]. As such, techniques for the visualization of the distribution of partial pressure of oxygen in tumors are of significant interest in pre-clinical and clinical research. To date, several non-invasive methods for oxygen-sensitive imaging have been reported, including near-infrared spectroscopy (NIRS) [2], fluorescence/phosphorescence imaging [3], positron emission tomography (PET) using hypoxia radiotracers [4], ^{19}F-magnetic resonance imaging (MRI) [5], blood oxygen level-dependent MRI [6], and electron paramagnetic resonance (EPR) imaging [7,8]. Of these imaging modalities, EPR is one of the few methods that enable quantitative visualization of the partial pressure of oxygen in tumors. In EPR-based oxygen mapping, the partial pressure of oxygen is typically measured from spectroscopic parameters such as the line-width of the absorption spectrum or the relaxation time of the unpaired electrons of an oxygen-sensitive spin probe. In pulsed EPR studies, a derivative of triarylmethyl radical, which has a relatively long relaxation time, is commonly used for oxygen mapping [9]. In contrast, continuous-wave (CW) EPR can be conducted with a variety of nitroxyl radicals as well as triarylmethyl radicals regardless of relaxation time.

The line-width of the EPR absorption spectrum and the relaxation time of unpaired electrons depend on both the concentration of the spin probe and the partial pressure of oxygen. Therefore, the influence of the probe concentration should be minimized to achieve quantitative measurements of the partial pressure of oxygen with high accuracy. In pulsed EPR, longitudinal relaxation time T_1-based oxygen mapping can provide pO_2 maps that are relatively less sensitive to the concentration of the spin probe than apparent transverse-relaxation time T_2^*-based pO_2 mapping [10,11]. In contrast to pulsed EPR, the oxygen-induced line broadening in CW-EPR spectra requires distinction from the spin probe

concentration-induced line broadening for pO_2 measurements, because the line-widths of first-derivative EPR absorption spectra in the CW detection method reflect relaxation time T_2^*, which is sensitive to the probe concentration as well as the partial pressure of oxygen.

To distinguish the effects of concentration-induced line broadening and the interaction with molecular oxygen on CW-EPR spectra, Halpern et al. used 4-protio-3-carbamoyl-2,2,5,5-tetraperdeuteromethyl-3-pyrrolinyl-1-^{15}N-oxy (mHCTPO) [12–14] as a spin probe and demonstrated non-invasive oxygen measurements by exploiting the hyperfine structure of mHCTPO in tumor animal models [14]. In their work, two parameters were derived from the EPR spectrum in order to determine the two unknowns; the probe concentration and the partial pressure of oxygen. However, processing of the hyperfine structure of the EPR spectrum at each voxel in the three-dimensional (3D) data space requires relatively time-consuming four-dimensional (4D) spectral-spatial imaging [15]. Precise 4D image reconstruction is critical for accurate measurements of spectral lines for pO_2 mapping [16].

In this work, we aimed to obtain two appropriate spectroscopic parameters for measurements of oxygen-induced line broadening in CW-EPR using a pair of ^{14}N- and ^{15}N-labeled nitroxyl radicals. In CW-EPR imaging, spectra pertaining to the ^{14}N- and ^{15}N-labeled nitroxyl radicals can be separated from the projection data measured from a mixture of the radicals under magnetic field gradients. This phenomenon has been previously reported [17,18], however, those works dealt with the EPR signal intensity only, rather than spectroscopic parameters such as the line-width or relaxation time T_2^*. Here we propose that simultaneous T_2^* mapping of ^{14}N- and ^{15}N-labeled nitroxyl radicals using single-point imaging (SPI) might meet the need of two spectroscopic parameters for the quantitative EPR measurement of oxygen-induced line broadening.

Thus, the goal of this work was to establish a method of simultaneous T_2^* mapping of

^{14}N- and ^{15}N-labeled nitroxyl radicals. The realization of this goal requires a process to separate the EPR spectra measured from a mixture of ^{14}N- and ^{15}N-labeled nitroxyl radicals. Herein, a local search method was applied to the CW-EPR imaging data to carry out this separation, and SPI was employed to enable simultaneous T_2^* mapping of a mixture of ^{14}N- and ^{15}N-labeled nitroxyl radicals in solution phantoms and living mice.

2. Methods

2.1. Spectral separation for ^{14}N- and ^{15}N-labeled nitroxyl radicals

The central concept behind our process of spectral separation is to find the spatial signal distribution of ^{14}N- and ^{15}N-labeled nitroxyl radicals in a mixture solution. Figure 1 shows the structure of a pair of ^{14}N- and ^{15}N-labeled nitroxyl radicals and the EPR spectrum for a mixture of those radicals. In this study, we consider that absorption spectra of each radical at low magnetic field (leftmost two peaks in Figure 1b) are simultaneously recorded with and without magnetic field gradients. After finding the spatial signal distribution for a given projection, each spectral projection can be computed by convolution of the spatial signal distribution and the corresponding zero-gradient spectrum of a mixture solution. Thus, to recover the spatial signal distribution, a process of deconvolution of the spectral projection and the zero-gradient spectrum is usually conducted. However, since it requires low-pass filtering to suppress the high-frequency noise and to avoid a division-by-zero problem, the reconstructed spatial distribution is typically blurred. To avoid blurring of the reconstructed spatial distribution, a process of deconvolution was not employed in the present work.

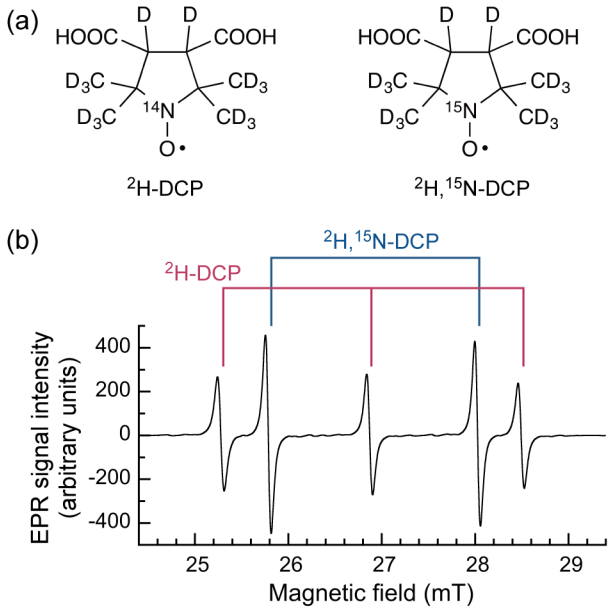

Fig. 1. Chemical structures of ^{14}N- and ^{15}N-labeled dicarboxy-PROXYLs and a representative EPR spectrum of a mixture of those nitroxyl radicals. (a) Chemical structure of ^{2}H-DCP and ^{2}H,^{15}N-DCP radicals, (b) EPR spectrum of a mixture of ^{2}H-DCP and ^{2}H,^{15}N-DCP radicals in solution. The probe concentrations were 2 mM for each radical.

To find the spatial distribution of the signals that are projected to the one-dimensional EPR spectra, we established the following optimization problem as a minimization of an evaluation function f, involving the measured spectrum under a magnetic field gradient $\boldsymbol{S}_{\mathrm{meas}}$, the computationally generated spectrum $\boldsymbol{S}_{\mathrm{comp}}$, and the spatial distribution of the signal $\boldsymbol{g}$:

$$\arg\min_{\boldsymbol{g}} f(\boldsymbol{g}), \quad (1)$$

where

$$f(\boldsymbol{g}) = \left\| \boldsymbol{S}_{\mathrm{meas}} - \boldsymbol{S}_{\mathrm{comp}} \right\|_2^2 + \lambda \left\| \nabla \boldsymbol{g} \right\|_{\mathrm{TV}}. \quad (2)$$

Here, the first term is the fidelity measure of the spectra (the sum of the squares of errors) and the second term is a regularization term. λ is a coefficient to control the regularization term, where TV stands for total variation norm for the spatial distribution of the projected signal:

$$\left\| \nabla \boldsymbol{g} \right\|_{\mathrm{TV}} = \sum_{i=1}^{n-1} \left| g_{i+1} - g_i \right|, \quad (3)$$

where n is size of the array $\boldsymbol{g}$, and g_i is the i-th component [19]. A process of convolution gives the computationally obtained spectrum $\boldsymbol{S}_{\mathrm{comp}}$:

$$\boldsymbol{S}_{\mathrm{comp}} = \boldsymbol{S}_{\mathrm{comp}}^{14\mathrm{N}} + \boldsymbol{S}_{\mathrm{comp}}^{15\mathrm{N}}, \quad (4)$$

$$\boldsymbol{S}_{\mathrm{comp}}^{14\mathrm{N}} = \boldsymbol{S}_{0}^{14\mathrm{N}} \otimes \boldsymbol{g}, \quad (5)$$

$$\boldsymbol{S}_{\mathrm{comp}}^{15\mathrm{N}} = \boldsymbol{S}_{0}^{15\mathrm{N}} \otimes \boldsymbol{g}, \quad (6)$$

where the symbol $\otimes$ denotes convolution, $\boldsymbol{S}_{\mathbf{0}}^{\mathbf{14N}}$ and $\boldsymbol{S}_{\mathbf{0}}^{\mathbf{15N}}$ are the zero-gradient spectra and $\boldsymbol{S}_{\mathbf{comp}}^{\mathbf{14N}}$ and $\boldsymbol{S}_{\mathbf{comp}}^{\mathbf{15N}}$ are the computed spectral projections for ^{14}N- and ^{15}N-labeled nitroxyl radicals, respectively.

To solve the optimization problem in Eq. (1), we implemented a gradient descent (GD)-based local search algorithm. Figure 2 shows a flowchart of the proposed algorithm for computing the separation of each spectral projection. Each GD iteration is formulated as:

$$g_i^{(k+1)} = g_i^{(k)} + \alpha \frac{\partial f\left[\boldsymbol{g}^{(k)}\right]}{\partial g_i^{(k)}}, \quad (7)$$

where α is a coefficient for updating the spatial distribution of the signals $\boldsymbol{g}$ for each iteration, which controls the speed of convergence, and superscript k denotes the iteration number. The non-negativity constraint was applied to array $\boldsymbol{g}$. To evaluate the convergence of the solution for each projection, we monitored the relative error e of the evaluation function f [Eq. (2)]:

$$e = \frac{f^{(k+1)} - f^{(k)}}{f^{(k+1)}}. \quad (8)$$

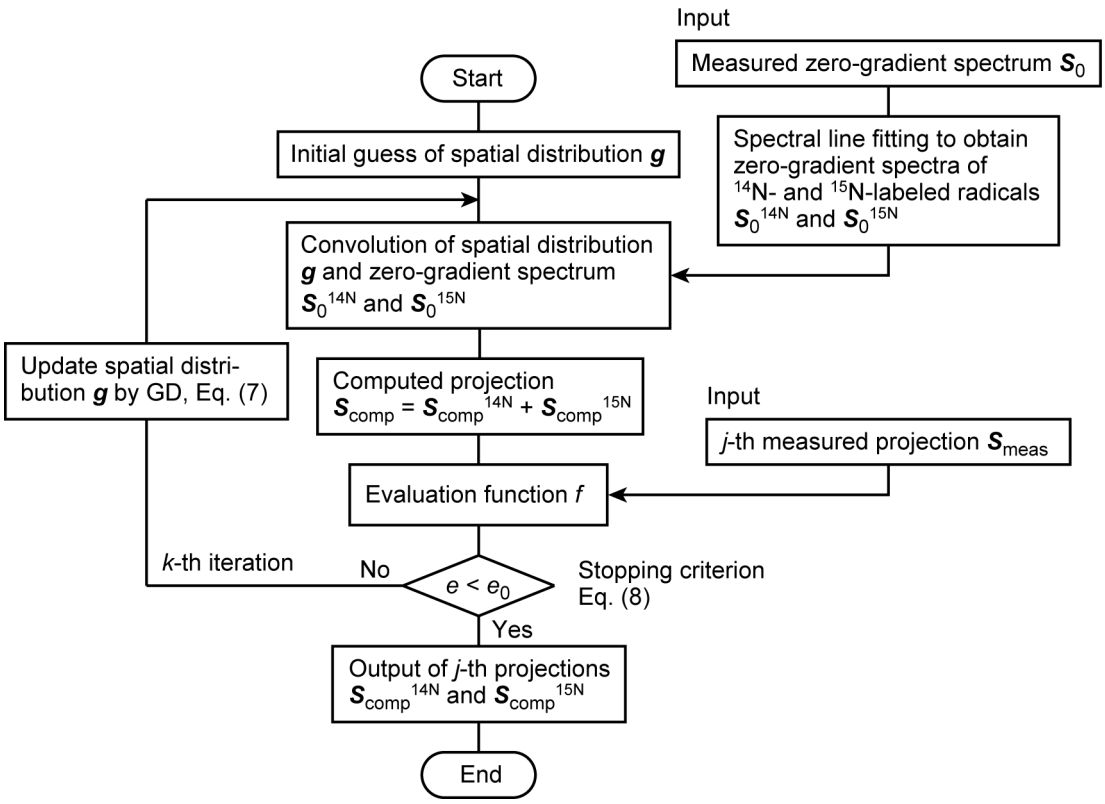

Fig. 2. Flowchart of the spectral projection separation process for ^{14}N- and ^{15}N-labeled nitroxyl radicals.

When this relative error was below a given threshold e_0, the process of iteration was terminated. We set the empirically optimized coefficients as follows: e_0=10^{-4}, α=10^{-4}, and λ=1.0. Coefficient λ was reduced to 0.15 when the relative error e approached e_0.

2.2. Image reconstruction and T_2^* mapping

The SPI method was used for image reconstruction of the spatial distribution and relaxation time T_2^* of the unpaired electrons [20–22]. Specifically, the acquired data (15 × 15 × 15 array) in the Fourier domain (*k*-space) were reformatted into a 64 × 64 × 64 or 32 × 32 × 32 array by zero padding, and a 3D spatial image was reconstructed by the 3D inverse Fourier transform using the subroutine of FFT3B in the IMSL Numerical Libraries (Rogue Wave Software, Louisville, CO). The field-of-view (FOV) of the reconstructed spatial image is

determined by the delay-time τ of free-induction decay (FID) detection under magnetic field gradients, given by:

$$\mathrm{FOV} = \frac{2\pi}{\gamma_e \tau \Delta G}, \quad (9)$$

where γ_e is the free-electron gyromagnetic ratio, and ΔG is the field gradient increment [21]. We computed the FID signal from the inverse Fourier transform (the FFTCB subroutine in the IMSL Numerical libraries) of an EPR absorption profile that was obtained by integration of the first-derivative EPR spectrum acquired by CW-EPR. The delay-time for FID detection was discretely set according to the sampling interval $\Delta\tau$, given as:

$$\Delta\tau = \frac{h}{g\beta\Delta B}, \quad (10)$$

where h is the Plank constant, g is the g-factor for the electron, β is the Bohr magneton, and ΔB is the width of magnetic field scan [22]. Specific parameters in our experiments are given in section 2.5. The effective spatial resolution of the reconstructed images was estimated from the 10%–90% distance in an edge-response curve of the image intensity profile after zero-padding the 1D signal profile to 1024 points.

To compute the relaxation time T_2^* at the voxel level, the FOV for the reconstructed images at different delay time-points was fixed using the *k*-space extrapolation method [23]. Multiple delay times were chosen to calculate T_2^* using a least-squares fitting method for the decay curve of the image intensities (see section 2.5). The effect of the Gaussian component was taken into account as well as the Lorentzian component (exponential decay) by using a Voigt function [24]. The signal decay curve s as a function of time t can thus be written as:

$$s(t) = Ke^{-at^2 - t/T_2^*}, \quad (11)$$

where K is the signal intensity at time $t = 0$. Coefficient a can be obtained from the full-width at half maximum (FWHM) of a Gaussian function

$$a = \frac{1}{2}\gamma_e{}^2\left(\frac{\mathrm{FWHM}}{2.35}\right)^2. \quad (12)$$

The FWHM of the Gaussian component was obtained by spectral fitting of the first-derivative EPR absorption spectrum using a Voigt function [24]. The 3D matrix size of T_2^* maps was 32 × 32 × 32. SPI-based image reconstruction and relaxation time computation was implemented using the Absoft Pro Fortran 2016 development environment (Rochester Hills, MI). Surface rendering was conducted using IDL version 8.4 (Exelis Visualization Information Solutions, Boulder CO). Two-dimensional images were visualized using ImageJ 1.50c (National Institutes of Health, Bethesda, MD, http://imagej.nih.gov/ij).

2.3. Chemicals

A pair of nitrogen-labeled nitroxyl radicals was used as oxygen-sensitive probes. The nitroxyl radicals,
trans-3,4-dicarboxy-2,2,5,5-tetra($^2H_3$)methylpyrrolidin-(3,4-$^2H_2$)-(1-^{15}N)-1-oxyl (^{2}H,^{15}N-DCP) and *trans*-3,4-dicarboxy-2,2,5,5-tetra($^2H_3$)methylpyrrolidin-(3,4-$^2H_2$)-1-oxyl (^{2}H-DCP) (see Fig. 1a), were synthesized as previously reported [25].

2.4. Solution phantoms

Two types of solution phantoms were prepared for proof-of-concept experiments of the separation of spectral projections and simultaneous T_2^* mapping.

(i) The first phantom was used for demonstration of the process of spectral separation and evaluation of reconstructed spectra and images. ^{2}H-DCP (2 mM) and ^{2}H,^{15}N-DCP (2 mM) were dissolved in phosphate buffered saline (PBS) and the solution pH was adjusted to 7.3 pH units by adding NaOH. The mixture was filled into a sample cell constructed from REXOLITE® 1422, cross-linked polystyrene, with an inner-cross section of 10 mm × 10 mm

and a length of 25 mm. The cap of the cell was made of DURACON®, engineering plastic polyoxymethylene. The volume of the mixture solution was 2.5 mL. Figure 3a shows a photograph of the cell containing a mixture solution of ^{2}H-DCP and ^{2}H,^{15}N-DCP.

(ii) The second phantom was used for simultaneous T_2^* mapping of the mixture solution of the probes, in which the dissolved oxygen fraction was altered by bubbling in gas mixtures of oxygen and nitrogen. The same 2 mM mixture solution of ^{2}H-DCP and ^{2}H,^{15}N-DCP dissolved in PBS (2.0 mL) was filled into a glass vial (14 mm inner diameter, 4 mL total volume). Separately, a mixture solution of ^{2}H-DCP (3 mM) and ^{2}H,^{15}N-DCP (3 mM) was prepared in order to investigate the influence of concentration on T_2^* mapping. Prior to EPR measurements, the mixture solution was bubbled with pure N_2 gas (oxygen free condition) or 5% O_2 and 95% N_2 gas mixture (oxygenated condition) to purge the air in the solution. A polytetrafluoroethylene tube was used to introduce gas into the solution in the vial, which was placed in an airtight plastic chamber. The flow rate of gas bubbling was set at 150 mL/min and monitored by a gas flow sensor (FD-A1, Keyence Corp., Osaka, Japan). Gas bubbling was performed for 5 min before each measurement. In preliminary tests, we confirmed that the T_2^* of the radical solution is maintained throughout the experiment duration when using a vial with a tightly sealed screw cap, as opposed to a flame-sealed glass tube. Figure 5a shows a photograph of the vial partially filled with a mixture solution of radicals.

2.5. In vitro imaging

To demonstrate the spectral separation method and simultaneous T_2^* mapping *in vitro*, the mixture solutions of ^{2}H-DCP and ^{2}H,^{15}N-DCP described above were visualized using a home-built 750-MHz CW-EPR imager (see section 2.7) with the following settings: scan time 100 ms, magnetic field scanning width ΔB 1.5 mT, magnetic field modulation 40 μT, modulation frequency 90 kHz, time-constant of lock-in amplifier 0.1 ms, number of data

acquisition points 512 per scan, and incident RF power 18 mW. Field gradients were incrementally ramped in equal steps for EPR image acquisition. Projections were acquired for 15 × 15 × 15 field gradients for the X-, Y-, and Z-directions (total of 3375 projections). The total acquisition time was 7.5 min. The maximum field gradient for each direction was 30 mT/m and hence the field gradient increment ΔG was 30/7 mT/m = 4.29 mT/m (15 equal steps; zero ±7 steps). Since the width of magnetic field scanning was 1.5 mT, the sampling interval $\Delta\tau$ of the FID signal becomes 23.8 ns [Eq. (10)] after inverse discrete Fourier transform of the EPR absorption spectrum. Therefore, we set the delay-times for FID detection to be integer multiples of the sampling interval $\Delta\tau$; 23.8, 47.6, 95.2, 142.8, and 214.2 ns were chosen to calculate T_2^*. Since the signal decay curve [Eq. (11)] is close to exponential decay, we empirically chose to sample a greater number of short delay times. We chose the latest delay time (214.2 ns) to obtain an appropriate FOV (38.8 mm) of the resultant image [Eq. (9)].

The interval of spectral data acquisition was 130 ms. This interval is the sum of the spectral acquisition time (100 ms) and additional time (30 ms) to control magnetic field scanning, which includes the time taken for the external magnetic field to return to its initial value and the time required for a linear field scan before and after the spectral data acquisition. During this additional time, the magnetic field gradients were set for three directions and stabilized.

2.6. In vivo imaging of tumor-bearing mice

To demonstrate the feasibility of simultaneous T_2^* mapping of ^{2}H-DCP and ^{2}H,^{15}N-DCP *in vivo*, tumor-bearing mice were scanned and individual images of ^{2}H-DCP and ^{2}H,^{15}N-DCP were reconstructed. All animal experiments were performed in accordance with the “Law for The Care and Welfare of Animals in Japan” and approved by the Animal Experiment

Committee of Hokkaido University (approval no. 15-0120). Six-week-old C3H/HeJ male mice (20–22 g) were purchased from Japan SLC (Hamamatsu, Japan). Murine squamous cell carcinoma (SCC VII) cells were subcutaneously injected into the right hind leg as reported previously [26]. EPR imaging was performed 8 or 9 days after the implantation of SCC VII cells (when tumor size was more than 10 mm). Mice were anesthetized by the inhalation of 1–2% isoflurane and the tail vein was cannulated. Mice were placed onto a dedicated holder, and the tumor-bearing leg was inserted into the resonator of the EPR imager. A mixture of ^{2}H-DCP and ^{2}H,^{15}N-DCP (0.8 mmol/kg body weight for each radical, 8 μL/g body weight for 100 mM ^{2}H-DCP and 100 mM ^{2}H,^{15}N-DCP mixture in 5 mM PBS) was intravenously injected as a bolus. Cytotoxicity tests of ^{2}H-DCP and the time course of EPR signals of both probes in tumors have been reported previously [26]. EPR image acquisition was started 5 minutes after injection. The mouse body temperature and respiration rate were monitored using a small animal monitoring and gating system (model 1030, SA Instruments, Inc., Stony Brook, NY). The mouse body temperature was maintained at approximately 37ºC by feedback-regulated heated airflow. The measurement settings for *in vivo* mouse imaging were identical to those for the solution phantoms detailed above (total acquisition time 7.5 min). To reduce the influence of erroneous T_2^* values associated with low SNR data, T_2^* was only calculated for voxels with a signal intensity greater than 30% of that of the maximum.

2.7. CW-EPR spectrometer/imager

A home-built CW-EPR spectrometer/imager operating at 750-MHz was used for EPR imaging of solution samples and tumor-bearing mice, details of which have been reported previously [27,28]. In brief, a permanent magnet (static magnetic field of 27 mT) and three sets of magnetic field gradients were used. The coils for magnetic field scanning were used in combination with the permanent magnet for EPR spectroscopy and imaging. A multi-coil

parallel-gap resonator (22 mm inner diameter and 30 mm length) was used to apply the RF magnetic field to the sample [27,29]. The measured conversion efficiency of the RF magnetic field was 44 $\mu T/W^{1/2}$ at the center of the resonator when the resonator was empty.

2.8. Magnetic resonance imaging

To evaluate the presence of bubbles in the sample volume and provide a standard with which to compare the EPR signal intensity distribution, ^{1}H magnetic resonance imaging was performed. A 1.5 T permanent magnet system was used with a home-built ^{1}H coil, and a Japan REDOX spectrometer (Japan REDOX Ltd., Fukuoka, Japan). Conventional 2D gradient echo images were acquired in all three orthogonal planes with a FOV of 39 mm × 39 mm, in order to match EPR images. Other sequence parameters were set as follows: acquisition matrix 128 × 128, slice thickness 2.5 mm, flip angle 20°, echo/repetition time (TE/TR) 9/100 ms, number of averages 4.

3. Results and Discussion

3.1. Separation of spectral projections

The solution phantom (i) (see Fig. 3a) was measured under air saturation to demonstrate the separation process of spectral projections for ^{2}H-DCP and $^{2}H,^{15}N$-DCP. Surface-rendered SPI-reconstructed images for each probe are shown in Fig. 3b. Figure 3c shows representative measured spectra (black) and the corresponding computed spectra (red) of the solution phantom for three magnetic field gradients G = 0.0, 12.9, and 21.4 mT/m. The same magnetic field gradients were applied in three orthogonal directions ($G_x = G_y = G_z = G$). Figure 3d shows the corresponding spatial distributions of the EPR signals. Note that the horizontal axis shows the data point number rather than the position in real space. Figure 3e shows the individual spectral projections resulting from the separation of the measured spectra in Fig.

3c.

The computationally derived spectral projections agreed well with the measured projections as shown qualitatively in Fig. 3c. From visual assessment of the 3D image reconstruction (Fig. 3b) and separated spectra (Fig. 3e), we concluded that the separation of spectral projections was adequately performed under several magnetic field conditions. For the separation process, we used the same zero-gradient spectra of ^{2}H-DCP and ^{2}H,^{15}N-DCP for all measured projections; i.e., we assumed a space-invariant (shift-invariant) image system [c.f. Eqs. (5) and (6)]. It is appropriate to consider a solution phantom as a space-invariant system, since the distribution of oxygen and the spin probes is approximately homogeneous. However, when we measure live mice, the distribution of oxygen and the concentration of probes are not homogeneous, and thus the measured system is no longer space-invariant for the zero-gradient spectra in the strict sense. Nevertheless, we note that the computationally derived spectral projections can be adapted to the measured spectra. The effect of a change in zero-gradient spectra at each point is mostly compensated for adapting the projected profile of EPR signals ($\boldsymbol{g}$) due to the fidelity term in Eq. (2). Even if the adapted projection profile slightly differs from the actual distribution of a corresponding projection, the process of image reconstruction is not obstructed. This is because the SPI method uses the computationally derived spectra ($\boldsymbol{S}_{\mathrm{comp}}^{14\mathrm{N}}$ and $\boldsymbol{S}_{\mathrm{comp}}^{15\mathrm{N}}$) for its image reconstruction, instead of the projected spatial distribution. According to the results shown in Fig. 3, we concluded that our optimization-based separation process for EPR absorption peaks worked well.

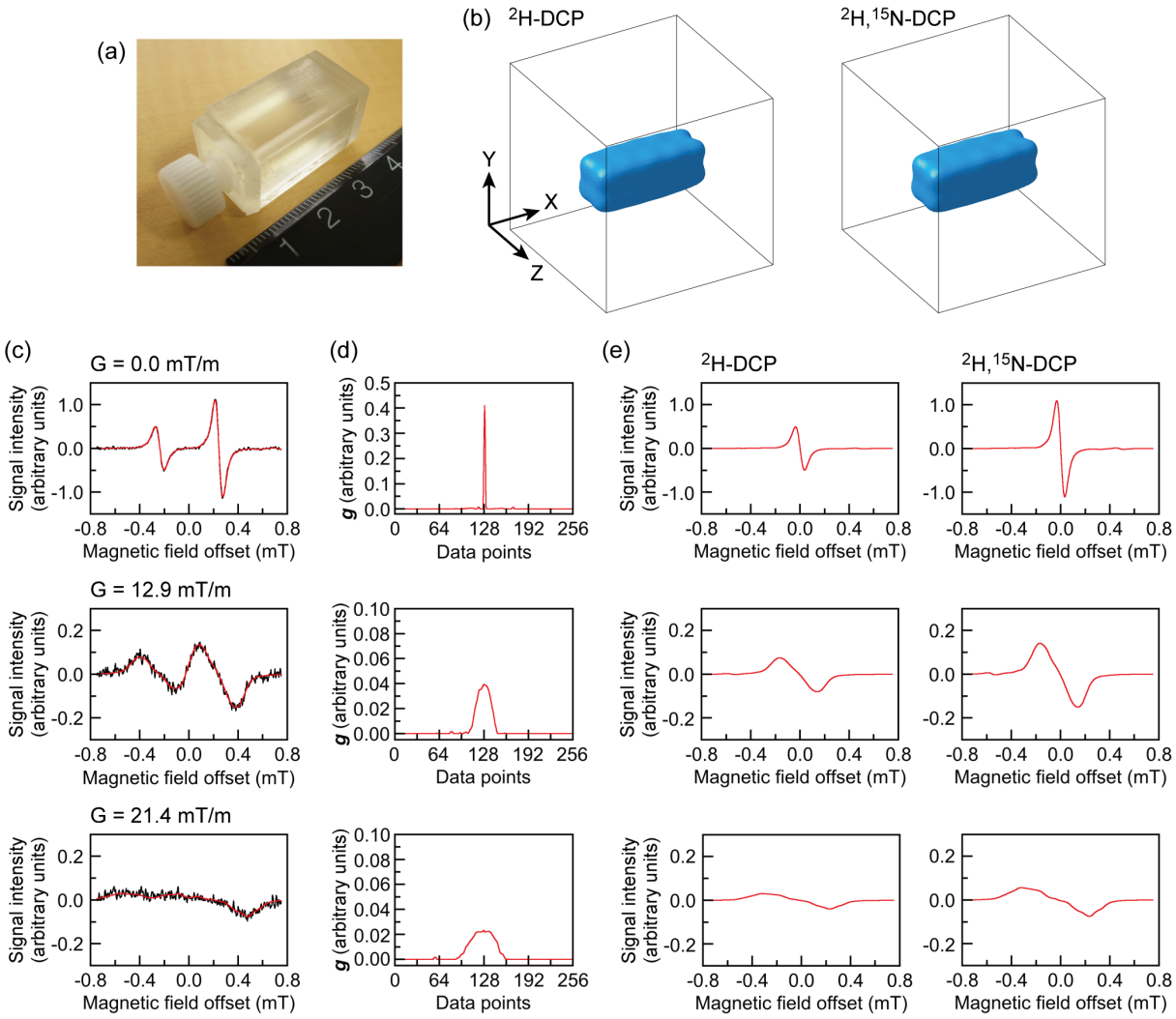

Fig. 3. Spectral separation of EPR spectra of ^{2}H-DCP and ^{2}H,^{15}N-DCP. (a) Photograph of the sample cell (i), (b) surface-rendered EPR images of ^{2}H-DCP and ^{2}H,^{15}N-DCP, (c) representative EPR spectra under magnetic field gradients G = 0.0, 12.9, and 21.4 mT/m, (d) spatial distribution of EPR signals in data point number, and (e) separated spectral projections of ^{2}H-DCP and ^{2}H,^{15}N-DCP.

3.2. Estimation of spatial resolution of reconstructed images

To estimate the spatial resolution of the reconstructed images, slice-selective intensity maps of ^{2}H-DCP and ^{2}H,^{15}N-DCP were analyzed. Figures 4a and 4b show ^{1}H MR images of the solution phantom as a reference in two orthogonal planes. Figures 4c and 4d (4e and 4f) present 2D slice-selective maps of the EPR signal intensity of ^{2}H-DCP (^{2}H,^{15}N-DCP), which

qualitatively reflect the shape of the solution in the cell on MRI. However, since the *k*-space data for EPR images is band-limited, fluctuation of image intensity was observed in the maps in Figs. 4c to 4f (c.f. surface-rendered images in Fig. 3b).

Figure 4g shows a representative spatial profile of the EPR image intensity along the gray dashed line in Fig. 4f, to illustrate the calculation of the 10%–90% distance for estimating spatial resolution. Figure 4h shows box-and-whisker plots of the 10%–90% distance at 20 distinct locations for the maps in Figs. 4d and 4f. The median 10%–90% distances of the ^{2}H-DCP map and the ^{2}H,^{15}N-DCP map were 2.70 mm and 2.69 mm, respectively, and there was no statistically significant difference between the mean spatial resolutions (two-tailed Student *t*-test, P=0.859, n=20). In summary, we concluded that the spectral projection separation process does not affect the spatial resolution of reconstructed images.

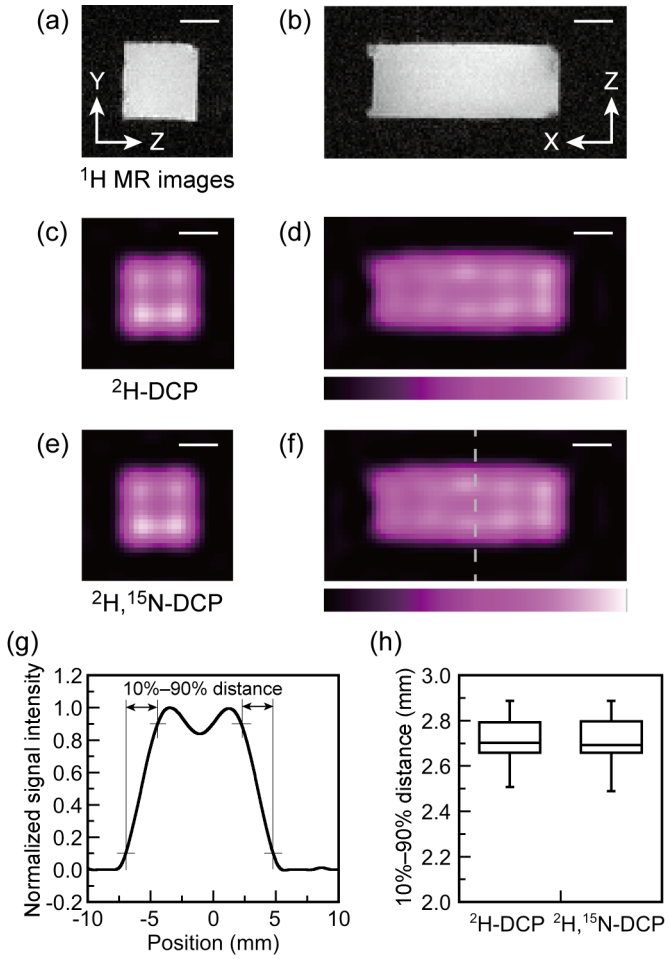

Fig. 4. Evaluation of reconstructed EPR signal intensity maps of the rectangular solution phantom. (a, b) ^{1}H MR images of the solution phantom in two orthogonal planes at the center of the phantom, (c, d) slice-selective EPR signal intensity maps of ^{2}H-DCP in the two orthogonal planes at the center of the phantom, and (e, f) corresponding EPR signal intensity maps of ^{2}H,^{15}N-DCP. (g) Spatial profile of the EPR signal intensity along the gray dashed line in Fig. 4f. (h) Box-and-whisker plots of the 10%–90% distance of the edge-response curve at 20 locations for the maps in Figs. 4d and 4f. Scale bars represent 5 mm.

3.3. In vitro T_2 mapping of solution samples*

Figure 5b presents a surface-rendered image of the EPR signal intensity of ^{2}H,^{15}N-DCP in the vial (photograph in Fig. 5a). Furthermore, Figs. 5c and 5d, and Figs. 5e and 5f, show slice-selective T_2^* maps of ^{2}H-DCP and ^{2}H,^{15}N-DCP in the oxygen-free condition and after bubbling of 5% O_2 and 95% N_2 gas mixture (oxygen condition; pO_2 = 38 mmHg),

respectively for a 2 mM probe concentration. The peak-to-peak line-widths of the first-derivative Lorentzian component of the zero-gradient EPR spectra measured from the solution phantom (probe concentration 2 mM) for ^{2}H-DCP and ^{2}H,^{15}N-DCP were 42.1 μT and 34.7 μT in the oxygen-free condition, respectively. Also, the FWHMs of the Gaussian component for ^{2}H-DCP and ^{2}H,^{15}N-DCP were 43.6 μT and 43.2 μT in the oxygen-free condition, respectively. These FWHM values were used in the computation of T_2^* using Eq. (11).

A reduction in T_2^* values of the probes can be seen as a shift in color on the T_2^* maps. To further highlight the reduction in T_2^* values in a quantitative manner, Figs. 5g and 5h show histograms of the T_2^* values of ^{2}H-DCP and ^{2}H,^{15}N-DCP for oxygen-free (blue bars) and 5% oxygen (red bars) conditions. Estimated T_2^* values were 150.3 ± 2.6 ns for ^{2}H-DCP and 178.7 ± 3.8 ns for ^{2}H,^{15}N-DCP for the oxygen-free condition; and 134.2 ± 2.5 ns for ^{2}H-DCP and 157.6 ± 4.2 ns for ^{2}H,^{15}N-DCP for the 5% oxygen condition (mean ± standard deviation of each 3D T_2^* map). These measurements indicate that the relaxation time T_2^* is a sensitive marker of dissolved oxygen in the solution.

Figure 6 presents slice-selective T_2^* maps (panel a–d) and the histograms of T_2^* values (panel e, f) of ^{2}H-DCP and ^{2}H,^{15}N-DCP for oxygen-free (blue bars) and 5% oxygen (red bars) conditions for a spin probe concentration of 3 mM. Estimated T_2^* values were 125.5 ± 2.2 ns for ^{2}H-DCP and 136.5 ± 3.0 ns for ^{2}H,^{15}N-DCP for the oxygen-free condition; and 119.7 ± 2.1 ns for ^{2}H-DCP and 129.9 ± 2.9 ns for ^{2}H,^{15}N-DCP for the 5% oxygen condition. The results shown in Figs. 5 and 6 indicate that the effects of both the concentration of the probes and dissolved oxygen in the solution on the relaxation time T_2^* can be quantitatively visualized. Thus, if calibration data of T_2^* as a function of the probe concentration and the oxygen partial pressure are obtained, the partial pressure of oxygen may be estimated more accurately by isolating the effect of concentration-induced relaxation.

T_2^* mapping with high accuracy requires a minimal standard deviation of the T_2^* values. Performing spatial filtering, e.g., with a moving average filter or median filter, can help reduce the scatter of T_2^* values. However, no filtering was applied to the T_2^* maps shown in Figs. 5 and 6. Additional factors affecting the scatter of T_2^* values may include the linearity of magnetic field scanning and gradients and the image reconstruction process itself. Therefore, all technical aspects should be appropriately optimized to enable minimal standard deviation of T_2^* values to aid the realization of the end goal of accurate oxygenation mapping with EPR. This optimization is a goal of present research in our laboratory.

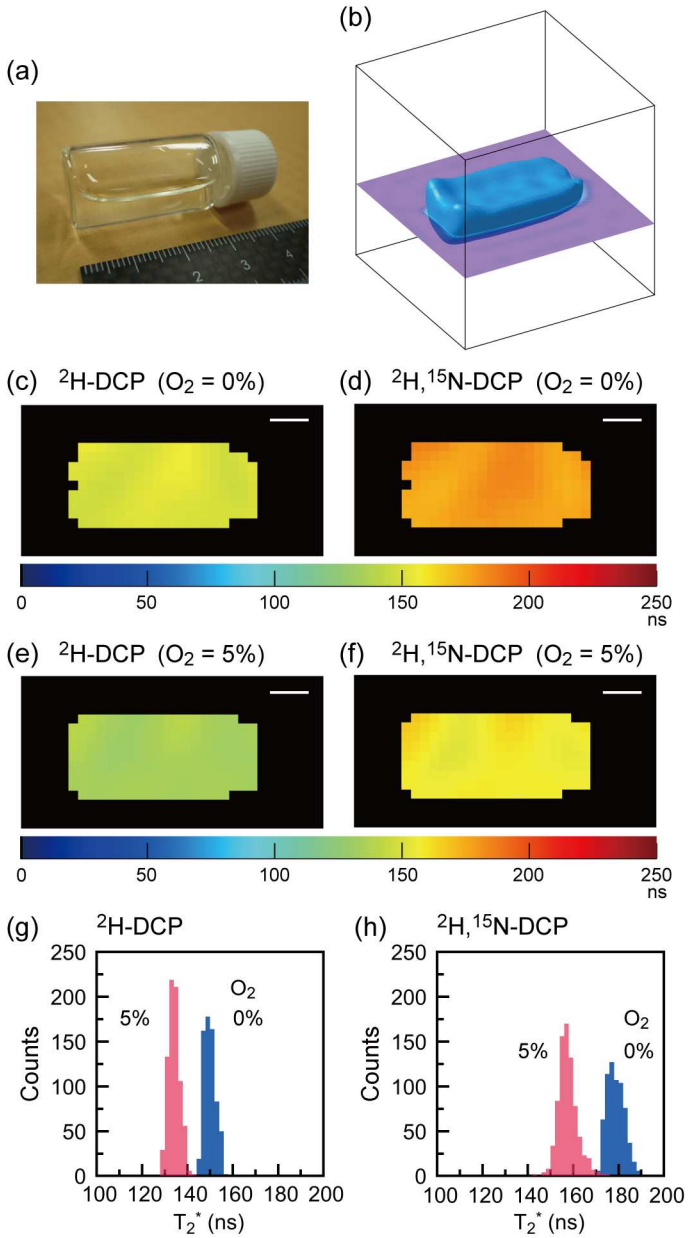

Fig. 5. Simultaneous T_2^* mapping of a mixture of ^{2}H-DCP (2 mM) and ^{2}H,^{15}N-DCP (2 mM). (a) Photograph of the vial partially filled with a mixture solution of the probes, (b) surface-rendered image of EPR signal intensity for ^{2}H,^{15}N-DCP (FOV 38.8 mm ×38.8 mm ×38.8 mm, image matrix 64 × 64 × 64), slice-selective T_2^* maps of each radical (c, d) after nitrogen bubbling (oxygen-free condition), and (e, f) after bubbling of 5% O_2 and 95% N_2 gas mixture (pO_2 = 38 mmHg), and (g, h) histograms of T_2^* values of ^{2}H-DCP and ^{2}H,^{15}N-DCP under the oxygen free and 5% oxygen conditions. The overlaid slice map in (b) indicates the position of slice-selective T_2^* maps. Blue bars indicate T_2^* values for the oxygen free condition and red bars indicate T_2^* values for the 5% oxygen condition in the histograms (bin width 2 ns). Scale bar represents 5 mm.

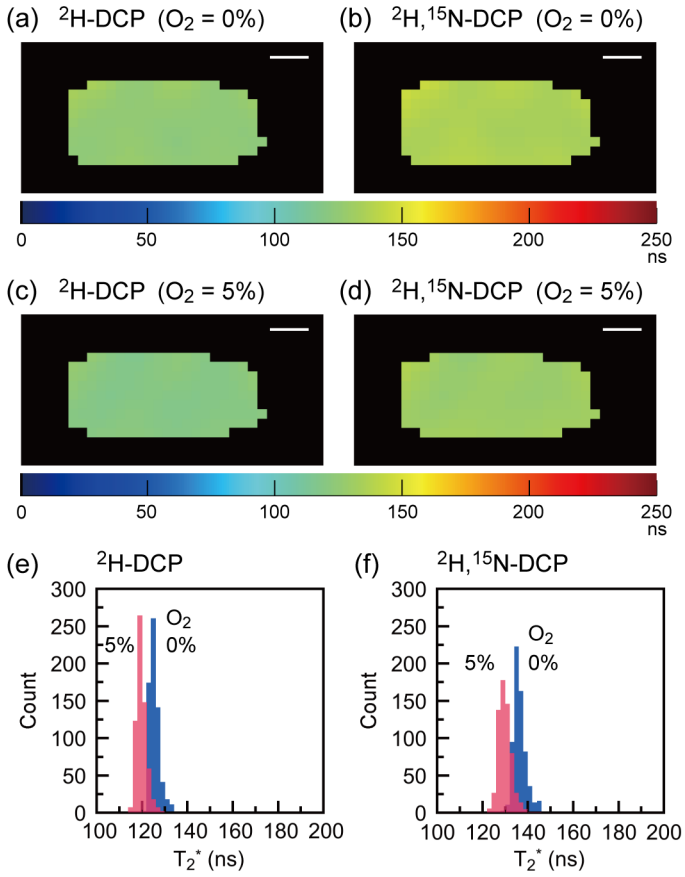

Fig. 6. Simultaneous T_2^* mapping of a mixture of ^{2}H-DCP (3 mM) and ^{2}H,^{15}N-DCP (3 mM). Slice-selective T_2^* maps of each radical (a, b) after nitrogen bubbling (oxygen-free condition), and (c, d) after bubbling of 5% O_2 and 95% N_2 gas mixture (pO_2 = 38 mmHg), and (e, f) histograms of T_2^* values of ^{2}H-DCP and ^{2}H,^{15}N-DCP under the oxygen free and 5% oxygen conditions. Scale bar represents 5 mm.

3.4. In vivo T_2 mapping of a mouse tumor model*

Figure 7a shows a photograph of a tumor-bearing mouse on the dedicated animal holder and Figure 7b shows a representative surface-rendered image of EPR signal intensity from ^{2}H,^{15}N-DCP in the tumor-bearing right hind leg of a representative mouse (body weight 24 g, tumor volume approximately 970 mm^3). Figures 7c and 7d and Figs. 7e and 7f show the slice-selective signal intensity maps and corresponding T_2^* maps, respectively, of ^{2}H-DCP and ^{2}H,^{15}N-DCP in the tumor-bearing hind leg.

An inhomogeneous distribution of EPR signals was observed, with a low signal intensity region in the center of the tumor. This may be attributed to insufficient delivery of the probes due to poor vasculature in the tumor microenvironment. Since the values of T_2^* were only calculated when the signal intensities at each voxel were above a given threshold, T_2^* values were not obtained in the low-signal intensity region in the center of the tumor. In the proximity of the signal void area in both T_2^* maps, prolonged T_2^* values were detected, which likely reflects a low concentration of the probes and/or a low partial pressure of oxygen. While pO_2 mapping was not performed in the current work, low-oxygen status in the same murine SCC VII tumors has been reported previously [30].

The results of simultaneous T_2^* mapping clearly show evidence of a successful spectral projection separation process in the tumor-bearing mouse hind leg. This mapping yields two spectroscopic parameters (T_2^* values) at a single voxel in the 3D image data, which we plan to use to generate pO_2 maps by employing appropriate calibration curves of the concentration-dependence and oxygen-dependence of the probes in the near future.

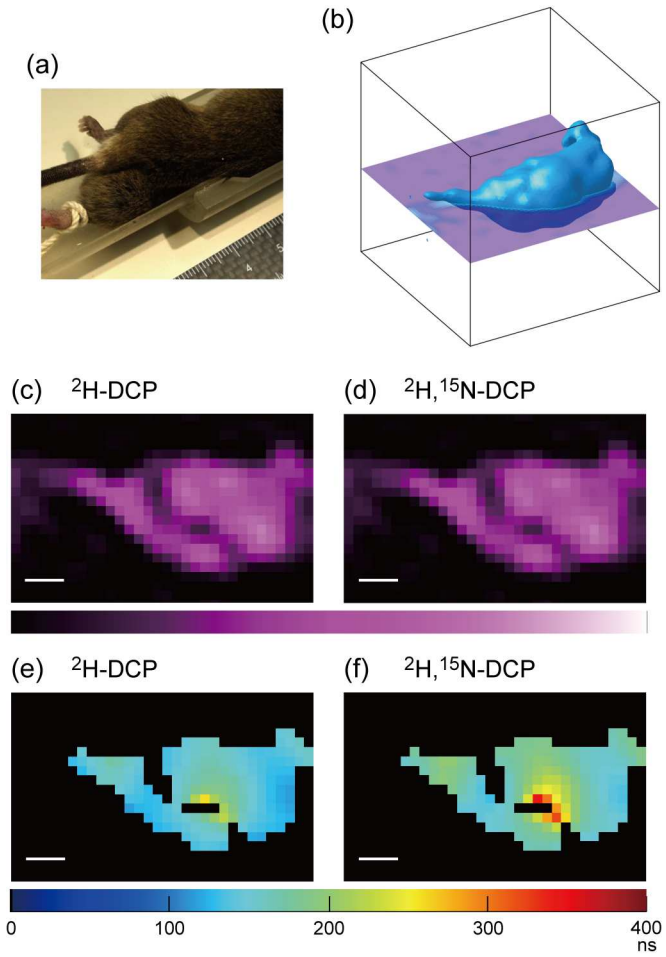

Fig. 7. Simultaneous T_2^* mapping of a mouse tumor-bearing hind leg. (a) Photograph of a subject mouse on the dedicated mouse holder, (b) surface-rendered image of EPR signals for ^{2}H,^{15}N-DCP, (c, d) slice-selective maps of EPR signal intensity for ^{2}H-DCP and ^{2}H,^{15}N-DCP in the coronal plane, and (e, f) corresponding T_2^* maps of ^{2}H-DCP and ^{2}H,^{15}N-DCP. FOV of the surface-rendered image (Fig. 7b) is 38.8 mm ×38.8 mm ×38.8 mm. The overlaid slice map in (b) indicates the position of slice-selective T_2^* maps (c–f). Scale bar represents 5 mm.

4. Conclusion

A method of simultaneous T_2^* mapping was established with CW-EPR-based SPI using ^{2}H-DCP and ^{2}H,^{15}N-DCP probes, employing a spectral projection separation process performed with a GD-based local search. Our experiments demonstrate that simultaneous 3D T_2^* mapping is feasible *in vitro* and *in vivo*. With further refinement, the presented T_2^* mapping approach should be extendable to enable quantitative oxygen mapping by CW-EPR

imaging.

Acknowledgments

The authors acknowledge Dr. Denis A. Komarov, Hokkaido University (presently The Ohio State University, the United States) for his assistance in the experiments. Also, the authors wish to express their gratitude to Kumiko Yamamoto, Dr. Hironobu Yasui, and Prof. Osamu Inanami, Graduate School of Veterinary Medicine, Hokkaido University for their assistance in the preparation of tumor-bearing mice. This work was supported by JSPS KAKENHI Grant Number JP26249057 (to H.H.) and Ministry of Education and Science of the Russian Federation, grant 14.W03.31.0034 (to I.A.K.). N.J.S. is a JSPS International Research Fellow.

References

[1] F. Colliez, B. Gallez, B.F. Jordan, Assessing tumor oxygenation for predicting outcome in radiation oncology: A review of studies correlating tumor hypoxic status and outcome in the preclinical and clinical settings, Front. Oncol. 7 (2017) 10, https://doi.org/10.3389/fonc.2017.00010.

[2] S. Jiang, B.W. Pogue, K.E. Michaelsen, M. Jermyn, M.A. Mastanduno, T.E. Frazee, P.A. Kaufman, K.D. Paulsen, Pilot study assessment of dynamic vascular changes in breast cancer with near-infrared tomography from prospectively targeted manipulations of inspired end-tidal partial pressure of oxygen and carbon dioxide, J. Biomed. Opt. 18 (2013) 076011, 10.1117/1.JBO.18.7.076011.

[3] T.C. O'Riordan, K. Fitzgerald, G.V. Ponomarev, J. Mackrill, J. Hynes, C. Taylor, D.B. Papkovsky, Sensing intracellular oxygen using near-infrared phosphorescent probes and live-cell fluorescence imaging, Am. J. Physiol. Regul. Integr. Comp. Physiol. 292 (2007) R1613–R1620, https://doi.org/10.1152/ajpregu.00707.2006.

[4] S.G.J.A. Peeters, C.M.L. Zegers, N.G. Lieuwes, W. van Elmpt, J. Eriksson, G.A.M.S. van Dongen, L. Dubois, P. Lambin, A comparative study of the hypoxia PET tracers [^{18}F]HX4, [^{18}F]FAZA, and [^{18}F]FMISO in a preclinical tumor model, Int. J. Radiat. Oncol. Biol. Phys. 91 (2015) 351–359, https://doi.org/10.1016/j.ijrobp.2014.09.045.

[5] M. Xia, V. Kodibagkar, H. Liu, R.P. Mason, Tumour oxygen dynamics measured simultaneously by near-infrared spectroscopy and ^{19}F magnetic resonance imaging in rats, Phys. Med. Biol. 51 (2006) 45–60, https://doi.org/10.1088/0031-9155/51/1/004.

[6] S. Ogawa, T. M. Lee, A.R. Kay, D.W. Tank, Brain magnetic resonance imaging with contrast dependent on blood oxygenation, Proc. Natl. Acad. Sci. USA 87 (1990) 9868–9872, https://doi.org/10.1073/pnas.87.24.9868.

[7] B. Epel, M. Kotecha, H.J. Halpern, In vivo preclinical cancer and tissue engineering

applications of absolute oxygen imaging using pulse EPR, J. Magn. Reson. 280 (2017)149–157, https://doi.org/10.1016/j.jmr.2017.04.017.

[8] S. Matsumoto, F. Hyodo, S. Subramanian, N. Devasahayam, J. Munasinghe, E. Hyodo, C. Gadisetti, J.A. Cook, J.B. Mitchell, M.C. Krishna, Low-field paramagnetic resonance imaging of tumor oxygenation and glycolytic activity in mice, J. Clin. Invest. 118 (2008) 1965–1973, https://doi.org/10.1172/JCI34928.

[9] J.H. Ardenkjær-Larsen, I. Laursen, I. Leunbach, G. Ehnholm, L.-G. Wistrand, J.S. Petersson, K. Golman, EPR and DNP properties of certain novel single electron contrast agents intended for oximetric imaging, J. Magn. Reson. 133 (1998) 1–12, https://doi.org/10.1006/jmre.1998.1438.

[10] B. Epel, M.K. Bowman, C. Mailer, H.J. Halpern, Absolute oxygen R_{1e} imaging in vivo with pulse electron paramagnetic resonance, Magn. Reson. Med. 72 (2014) 362–368, https://doi.org/10.1002/mrm.24926.

[11] K. Matsumoto, S. Kishimoto, N. Devasahayam, G.V.R. Chandramouli, Y. Ogawa, S. Matsumoto, M.C. Krishna, S. Subramanian, EPR-based oximetric imaging: a combination of single point-based spatial encoding and T_1 weighting, Magn. Reson. Med. (2018), https://doi.org/10.1002/mrm.27182.

[12] H.J. Halpern, M. Peric, T.D. Nguyen, D.P.J. Spencer, Selective isotopic labeling of a nitroxide spin label to enhance sensitivity for T_2 oxymetry, J. Magn. Reson. 90 (1990) 40–51, https://doi.org/10.1016/0022-2364(90)90364-F.

[13] H.J. Halpern, M. Peric, C. Yu, B.L.J. Bales, Rapid quantitation of parameters from inhomogeneously broadened EPR spectra, J. Magn. Reson. Ser. A 103 (1993) 13–22.

[14] H.J. Halpern, C. Yu, M. Peric, E. Barth, D.J. Grdina, B.A. Teicher, Oxymetry deep in tissues with low-frequency electron paramagnetic resonance, Proc. Natl. Acad. Sci. USA 91(1994) 13047–13051, https://doi.org/10.1073/pnas.91.26.13047.

[15] P. Kuppusamy, M. Chzhan, A. Samouilov, P. Wang, J.L. Zweier, Mapping the spin-density and lineshape distribution of free radicals using 4D spectral-spatial EPR imaging, J. Magn. Reson. Ser. B 107 (1995) 116–125, https://doi.org/10.1006/jmrb.1995.1067.

[16] D.A. Komarov, H. Hirata, Fast backprojection-based reconstruction of spectral-spatial EPR images from projections with the constant sweep of a magnetic field, J. Magn. Reson. 281 (2017) 44–50, https://doi.org/10.1016/j.jmr.2017.05.005.

[17] A. Pawlak, R. Ito, H. Fujii, H. Hirata, Simultaneous molecular imaging based on electron paramagnetic resonance of ^{14}N- and ^{15}N-labelled nitroxyl radicals, Chem. Commun. 47 (2011) 3245–3247, https://doi.org/10.1039/C0CC03581E.

[18] W. Takahashi, Y. Miyake, H. Hirata, Artifact suppression in electron paramagnetic resonance imaging of ^{14}N- and ^{15}N-labeled nitroxyl radicals with asymmetric absorption spectra, J. Magn. Reson. 247 (2014) 31–37, https://doi.org/10.1016/j.jmr.2014.08.001.

[19] A. Chambolle, An algorithm for total variation minimization and applications, J. Math. Imaging Vis. 20 (2004) 89–97, https://doi.org/10.1023/B:JMIV.0000011325.36760.1e.

[20] S. Choi, X.-W. Tang, D.G. Cory, Constant time imaging approaches to NMR microscopy, Int. J. Imaging Sys. Technol. 8 (1997) 263–276, https://doi.org/10.1002/(SICI)1098-1098(1997)8:3<263::AID-IMA4>3.0.CO;2-8.

[21] S. Subramanian, N. Devasahayam, R. Murugesan, K. Yamada, J. Cook, A. Taube, J.B. Mitchell, J.A.B. Lohman, M.C. Krishna, Single-point (constant-time) imaging in radiofrequency Fourier transform electron paramagnetic resonance, Magn. Reson. Med. 48 (2002) 370–379, https://doi.org/10.1002/mrm.10199.

[22] K. Matsumoto, B. Chandrika, J.A.B. Lohman, J.B. Mitchell, M.C. Krishna, S. Subramanian, Application of continuous-wave EPR spectral-spatial image reconstruction techniques for in vivo oxymetry: comparison of projection reconstruction

and constant-time modalities, Magn. Reson. Med. 50 (2003) 865–874, https://doi.org/10.1002/mrm.10594.

[23] H. Jang, S. Subramanian, N. Devasahayam, K. Saito, S. Matsumoto, M.C. Krishna, A.B. McMillan, Single acquisition quantitative single-point electron paramagnetic resonance imaging, Magn. Reson. Med. 70 (2013) 1173–1181, https://doi.org/10.1002/mrm.24886.

[24] S.N. Dobryakov, Ya. S. Lebedev, Analysis of a spectral line whose shape is described by a composition of Gauss's and Lorenz's distributions, Dokl. Akad. Nauk. SSSR 182 (1968) 68–70.

[25] A.A. Gorodetsky, I.A. Kirilyuk, V.V. Khramtsov, D.A. Komarov, Functional electron paramagnetic resonance imaging of ischemic rat heart: Monitoring of tissue oxygenation and pH, Magn. Reson. Med. 76 (2016) 350–358, https://doi.org/10.1002/mrm.25867.

[26] H. Kubota, D.A. Komarov, H. Yasui, S. Matsumoto, O. Inanami, I.A. Kirilyuk, V.V. Khramtsov, H. Hirata, Feasibility of in vivo three-dimensional T_2^* mapping using dicarboxy-PROXYL and CW-EPR-based single-point imaging, Magne. Reson. Mater. Phy. 30 (2017) 291–298, https://doi.org/10.1007/s10334-016-0606-8.

[27] H. Sato-Akaba, H. Fujii, H. Hirata, Improvement of temporal resolution for three-dimensional continuous-wave electron paramagnetic resonance imaging, Rev. Sci. Instrum. 79 (2008) 123701, https://doi.org/10.1063/1.3033161.

[28] H. Sato-Akaba, Y. Kuwahara, H. Fujii, H. Hirata, Half-life mapping of nitroxyl radicals with three-dimensional electron paramagnetic resonance imaging at an interval of 3.6 seconds, Anal. Chem. 81 (2009) 7501–7506, https://doi.org/10.1021/ac901169g.

[29] Y. Kawada, H. Hirata, H. Fujii, Use of multi-coil parallel-gap resonators for co-registration EPR/NMR imaging, J. Magn. Reson. 184 (2007) 29–38, https://doi.org/10.1016/j.jmr.2006.09.014.

[30] H. Yasui, S. Matsumoto, N. Devasahayam, J.P. Munasinghe, R. Choudhuri, K. Saito, S. Subramanian, J.B. Mitchell, M.C. Krishna, Low-field magnetic resonance imaging to visualize chronic and cycling hypoxia in tumor-bearing mice, Cancer Res. 70 (2010) 6427–6436, https://doi.org/10.1158/0008-5472.CAN-10-1350.